Intermittency in the isotropic component of helical and nonhelical turbulent flows

L. N. Martin[1] and P. D. Mininni[1,2]
[1]*Departamento de Física, Facultad de Ciencias Exactas y Naturales, Universidad de Buenos Aires and CONICET, Ciudad Universitaria, 1428 Buenos Aires, Argentina*
[2]*NCAR, P.O. Box 3000, Boulder, Colorado 80307-3000, USA*
(Received 6 July 2009; revised manuscript received 6 November 2009; published 14 January 2010)

We analyze the isotropic component of turbulent flows spanning a broad range or Reynolds numbers. The aim is to identify scaling laws and their Reynolds number dependence in flows under different mechanical forcings. To this end, we applied an SO(3) decomposition to data stemming from direct numerical simulations with spatial resolutions ranging from 64^3 to 1024^3 grid points, and studied the scaling of high order moments of the velocity field. The study was carried out for two different flows obtained forcing the system with a Taylor-Green vortex or the Arn'old-Beltrami-Childress flow. Our results indicate that helicity has no significant impact on the scaling exponents as obtained from the generalized structure functions. Intermittency effects increase with the Reynolds number in the range of parameters studied, and in some cases are larger than what can be expected from several models of intermittency in the literature. The observed dependence of intermittency with the Reynolds number decreases if extended self-similarity is used to estimate the exponents.

DOI: 10.1103/PhysRevE.81.016310 PACS number(s): 47.27.ek, 47.27.Ak, 47.27.Jv, 47.27.Gs

I. INTRODUCTION

Turbulence is a recurring phenomenon in nature; we can find turbulent dynamics in atmospheric, geophysical, and astrophysical flows. The dynamics of these flows is often described by identifying three characteristic ranges of scales [1]: the injection range, whose properties depend on the forcing; the inertial range, which is assumed to have universal properties in the limit of infinite Reynolds number; and the viscous range, where dissipation takes place. In three-dimensional isotropic and homogeneous turbulence, the scale separation between the forcing and the viscous range (i.e., the width of the inertial range) increases as a known power of the Reynolds number. Nowadays, computing power is scarcely sufficient to study in direct numerical simulations (DNS) flows with these three ranges well resolved. Even in the few simulations where an incipient scale separation is achieved [2–4], an exploration of the parameter space to build confidence on such assumptions as universality of inertial range properties is currently out of reach.

In a recent study [5] numerical simulations up to spatial resolutions of 1024^3 grid points were performed using different forcing functions, including coherent and delta correlated in time forcing, as well as using mechanisms that injected only energy or both energy and helicity into the flow. From numerical simulations [6–9] it is known that helical and nonhelical isotropic and homogeneous turbulence follows a Kolmogorov scaling in the inertial range, albeit intermittency corrections. However, in [5] a departure in the scaling exponents of higher order moments between helical and nonhelical simulations was found. It was unclear whether these departures were associated to a dependence with the helicity content of the flow, or with anisotropies generated by the different forcing functions acting on the large scale. Other studies reported a dependence of the intermittency of the energy flux [7], or dependence of the recovery of isotropy on helicity-dependent statistical quantities on the amplitude of the helicity flux [10]. Shell model studies [11] also reported subleading corrections to scaling laws associated to the presence of helicity.

In this work, we use the SO(3) decomposition [12,13] (see also [14] for a review) to separate the isotropic and anisotropic components of a turbulent flow. To deal with the size of our data sets, the method is implemented numerically as described in [15]. Previous studies focused on the scaling of the anisotropic sectors (see, e.g., [16–19]) from data stemming from numerical simulations or experiments, as it has been conjectured that both the isotropic and anisotropic sectors of turbulent flows may follow universal scaling laws in the inertial range (see, e.g., [13,19]), and as for the third order structure function it has been rigorously shown that the "four-fifth law" holds in the isotropic sector even in the presence of anisotropies [12,20]. A dimensional prediction for the scaling of the generic anisotropic sectors has also been put forward [19]. Evidence of possible universality of scaling laws in the anisotropic sector have been further obtained using the SO(3) decomposition in Rayleigh-Benard convection [21,22] and in the random Kolmogorov flow [23]. These studies also showed (albeit in simulations or experiments at moderate Reynolds numbers) that the use of the SO(3) decomposition improves the convergence of high order moments of the velocity field [13,18]. For the determination of just the third order scaling exponent, studies of the isotropic component have been done up to spatial resolutions of 512^3 grid points [15]. However, less attention has been paid to comparisons of the scaling exponents in the isotropic sector for orders other than second or third, and to comparisons of these exponents for different forcing functions in simulations at large spatial resolution. Considering the differences reported in helical and nonhelical turbulence, it seems reasonable to consider such flows for a comparison. Here, we use velocity fields stemming from six DNS with spatial resolutions ranging from 64^3 to 1024^3 grid points, using either helical or nonhelical forcing mechanisms. Velocity increments and scaling exponents in the inertial range are computed for all runs, up to eight order for the simulations with the larger spatial resolution.

The analysis indicates that helicity has no measurable effect on the scaling exponents of the velocity field, with the differences observed in the exponents stemming from the different runs being within error bars, ascribable to sensitivity to the fitting range, or to Reynolds number dependence. Moreover, we find that in some cases intermittency (as measured from the departure of the linear dependence of the scaling exponents with the order, associated to the development of strong events in the velocity field) increases with the Reynolds number in the range of parameters studied, indicating convergence of high order moments to their infinite Reynolds number limit is slow and may have not been achieved even in the largest numerical simulations up to date. The Reynolds number dependence decreases a little bit when extended self-similarity (ESS) [24,25] is used. Finally, our results are in agreement with previous studies showing that the use of the SO(3) decomposition improves scaling laws and the determination of scaling exponents.

The structure of the paper is as follows. Section II briefly describes the numerical simulations. Section III introduces the SO(3) decomposition and describes the method we use to apply the decomposition to our data, based on the method proposed in [15]. Section IV discusses the 4/5 law and the energy scaling in the isotropic sector of the velocity fields. Section V presents the scaling laws obtained in the inertial range for the different moments of the velocity field. Also, a comparison between helical and nonhelical flows is done, as well as a comparison with models of intermittency. Section VI is devoted to the analysis of the scaling exponents when ESS is used, and to a comparison of the exponents when absolute values are used in the definition of the structure functions or not. Finally, Sec. VII presents the conclusions.

II. NUMERICAL SIMULATIONS

The data sets we use for the analysis stem from DNS that solve the momentum equation for an incompressible fluid with constant mass density. The Navier-Stokes equations under these conditions read

$$\frac{\partial \mathbf{v}}{\partial t} + \mathbf{v}\cdot\boldsymbol{\nabla}\mathbf{v} = -\frac{\boldsymbol{\nabla} p}{\rho} + \mathbf{f} + \nu\nabla^2\mathbf{v}, \tag{1}$$

$$\boldsymbol{\nabla}\cdot\mathbf{v} = 0, \tag{2}$$

where $\mathbf{v}$ is the velocity field, p is the pressure, $\mathbf{f}$ is an external force that drives the turbulence, ν is the kinematic viscosity, and ρ is the mass density of the fluid (set to unity here in dimensionless units). The mode with the largest wave vector in the Fourier transform of $\mathbf{f}$ is defined as the forcing wave number k_f, with the forcing scale given by $L_f = 2\pi/k_f$.

Equations (1) and (2) are solved using a parallel pseudospectral code in a three-dimensional box of size 2π with periodic boundary conditions [26,27]. We use three different spatial resolutions: 64^3, 256^3, and 1024^3 grid points. The equations are evolved in time using a second order Runge-Kutta method, and the code uses the 2/3 rule for dealiasing. Reynolds numbers quoted are based on the integral scale and defined as $\mathrm{Re} = UL/\nu$, where $U = \langle v^2\rangle^{1/2}$ is the rms velocity and the integral scale L is defined as

TABLE I. Parameters used in the simulations. N is the linear resolution, $\mathbf{f}$ is the forcing (either TG or ABC), k_f is the forcing wave number, ν is the kinematic viscosity, and Re is the Reynolds number.

Run	N	$\mathbf{f}$	k_f	ν	Re
T1	64	TG	2	5×10^{-2}	40
T2	256	TG	2	2×10^{-3}	675
T3	1024	TG	2	3×10^{-4}	3950
A1	64	ABC	3	4×10^{-2}	70
A2	256	ABC	3	2×10^{-3}	820
A3	1024	ABC	3	2.5×10^{-4}	6200

$$L = 2\pi\frac{\int E(k)k^{-1}dk}{\int E(k)dk}, \tag{3}$$

with $E(k)$ the energy spectrum such that the total energy is $E = \int E(k)dk$.

We examine two different flows, generated by different volume forces $\mathbf{f}$ that are either nonhelical or fully helical (we consider a forcing function fully helical when $\langle \mathbf{f}\cdot\boldsymbol{\nabla}\times\mathbf{f}\rangle$ is maximal and nonhelical when $\langle \mathbf{f}\cdot\boldsymbol{\nabla}\times\mathbf{f}\rangle$ is zero, with the brackets denoting spatial average): the Taylor-Green (TG) vortex [4], and the Arn'old-Beltrami-Childress (ABC) flow [5]. The former is nonhelical, and the resulting flow has no net helicity, although spatially localized regions with positive or negative helicity develop. The latter is fully helical, and the resulting flow therefore has helicity (where the flow helicity is defined as $H = \langle \mathbf{u}\cdot\boldsymbol{\nabla}\times\mathbf{u}\rangle$) [28,29].

When using the TG vortex as a forcing function, we prescribe $\mathbf{f}$ as

$$\mathbf{f}_{TG} = f_0[\sin(k_f x)\cos(k_f y)\cos(k_f z)\hat{x} - \cos(k_f x)\sin(k_f y)\cos(k_f z)\hat{y}], \tag{4}$$

while the ABC forcing is given by

$$\mathbf{f}_{ABC} = f_0\{[B\cos(k_f y) + C\sin(k_f z)]\hat{x} + [A\sin(k_f x) + C\cos(k_f z)]\hat{y} + [A\cos(k_f x) + B\sin(k_f y)]\hat{z}\}. \tag{5}$$

Here f_0 is the forcing amplitude, which was set to have in the turbulent steady state all runs with rms velocities near unity. For ABC forcing, the constants were chosen to be $A=0.9$, $B=1$, and $C=1.1$. Table I shows the parameters for all the runs. More details about the runs, and a detailed analysis of energy spectra, fluxes, and energy transfer, can be found in [5,30].

III. SO(3) DECOMPOSITION

The isotropic component of the longitudinal velocity structure functions for each flow is extracted using the SO(3) decomposition following the method described in [15]. Some modifications were made considering the size of our simulations and to obtain a parallel version compatible with the way data is distributed among computing nodes. In this section we briefly introduce the method described in [15] and give details of our implementation.

To do the SO(3) decomposition and recover the isotropic component, the longitudinal velocity structure function of order p is decomposed in terms of the spherical harmonics Y_{lm}, obtaining

$$S_p(\mathbf{l}) = \langle \{[\mathbf{v}(\mathbf{r}) - \mathbf{v}(\mathbf{r}+\mathbf{l})] \cdot \hat{l}\}^p \rangle = \sum_{jm} S_p^{jm}(l) Y_{jm}(\hat{l}), \quad (6)$$

where the brackets denote spatial average over the variable $\mathbf{r}$, and homogeneity is assumed. The coefficients S_p^{jm} are obtained by projecting $S_p(\mathbf{l})$ into the spherical harmonics, or equivalently, by projecting the pth power of the longitudinal increments

$$\delta v(\mathbf{r},\mathbf{l}) = [\mathbf{v}(\mathbf{r}) - \mathbf{v}(\mathbf{r}+\mathbf{l})] \cdot \hat{l} \quad (7)$$

into the spherical harmonics and averaging over $\mathbf{r}$. We are interested in the isotropic sector, given by the $S_p^{00}(l)$ functions,

$$S_p^{00}(l) = \frac{1}{4\pi} \left\langle \int_0^{2\pi} \int_0^{\pi} \delta v^p(\mathbf{r},\mathbf{l}) l^2 \sin(\varphi) d\varphi d\theta \right\rangle, \quad (8)$$

where the angles φ and θ are associated to the vector $\mathbf{l}$. It is also useful to introduce the generalized structure functions $G_p(\mathbf{l}) = \langle |[\mathbf{v}(\mathbf{r}) - \mathbf{v}(\mathbf{r}+\mathbf{l})] \cdot \hat{l}|^p \rangle$ using the absolute value of the longitudinal increments (see, e.g., [31]). It has been reported [24,25] that both G_p and S_p follow scaling laws, although the use of absolute values in G_p increases the range of scales where power laws are observed. In the following, we will use G_p for all runs in Table I, and S_p to compare when possible (see Sec. VI for more details). G_p can be decomposed as S_p into its isotropic component G^{00} using the absolute value of the velocity increments in Eq. (8).

The discrete version of the Eq. (8), and therefore the expression used in the numerical code to carry out the decomposition, is

$$S_p^{00}(l) = \frac{1}{N_d N^3} \sum_{j=1}^{N_d} \sum_{i=1}^{N^3} \delta v^p(\mathbf{r}_i,\mathbf{l}_j), \quad (9)$$

where N is the linear resolution and N_d is the number of directions used to compute the average over the sphere.

In Ref. [15] it was shown that 146 different directions $\mathbf{l}_j$ covering in an approximately uniform way the sphere can be generated on a regular grid in such a way that all integer multiples of $\mathbf{l}_j$ lie on a grid point. This avoids the need to use three-dimensional interpolations to compute the longitudinal increments $\delta v(\mathbf{r}_i,\mathbf{l}_j)$ when $\mathbf{r}+\mathbf{l}$ does not lie on a grid point, significantly reducing the computational cost of the decomposition. The 146 directions are generated by the vectors (1,0,0), (1,1,0), (1,1,1), (2,1,0), (2,1,1), (2,2,1), (3,1,0), (3,1,1) and those that are obtained by permuting their components in every possible way (including multiplication of the vectors by −1). With periodic boundary conditions, negative multiples of the vectors are not needed, since a spatial average over the entire box with the increment $\mathbf{l}_j$ gives the same result as the average with $-\mathbf{l}_j$. This reduces N_d in Eq. (9) to 73.

The code we use to solve the Navier-Stokes equations is parallelized using a two-dimensional domain decomposition [26,27]. Each computing node stores a slice of the velocity field in real space of size $N \times N \times N_z$ ($N_z \leq N$, with N_z a function of the number of computing nodes). As a result, increments in Eq. (9) in the x and y directions can be computed locally in each node. However, increments in the z direction require communication which is handled using the message passing interface (MPI) library. The sum in Eq. (9) is then computed as follows: for each increment $\mathbf{l}_j$, displacements of the velocity field in the x and y direction are computed. Communication is then performed to displace the velocity field in the z direction if needed, and $\delta v(\mathbf{r}_i,\mathbf{l}_j)$ is computed for all values of $\mathbf{r}_i$. Finally, the sum over all $\mathbf{r}_i$ is done. The process is repeated for integer multiples of $\mathbf{l}_j$ by just displacing the already displaced velocity field on $\mathbf{l}_j$ over and over again. In this way, all communications are done between nearest neighbors avoiding all-to-all communications.

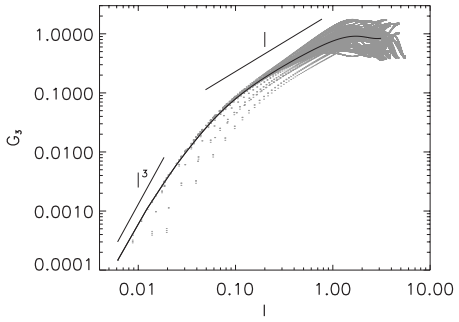

FIG. 1. Third order structure functions $G_3(\mathbf{l})$ and isotropic component $G_3^{00}(l)$ as a function of l for the T3 (nonhelical) run. Gray dots correspond to the 73 different directions while the thick solid line is the $G_3^{00}(l)$ average. The straight lines indicate $\sim l^3$ and $\sim l$ scaling.

IV. 4/5 LAW AND THE ENERGY SPECTRUM

The result of computing the generalized third order structure functions for the 73 directions using the T3 data set is shown in Fig. 1. The average over all directions (computed using a procedure similar to the one described in [15]) is also shown. From the 4/5 law [32], we expect the third order structure function to scale as the increment l in the inertial range. This is indeed the case for the average (the isotropic component) in a wide range of scales (even using the absolute value), while the structure function in each direction may or may not follow this law. In the dissipative range, where the flow becomes regular, a scaling $\sim l^3$ is observed for all curves.

That the generalized third order structure function scales as $\sim l$ in the inertial range has been observed before [31]. However, to see if the data is consistent with the 4/5 law the structure functions $S_3(l)$ and S_3^{00} must be computed. This is shown in Fig. 2, which presents the third order structure function compensated by ϵl. The amplitude of $S_3^{00}(l)$ in the inertial range is close to the expected $-4\epsilon l/5$ value.

At lower Reynolds number (and spatial resolution) scaling in the inertial range can still be identified although the width of the scaling range decreases. This is illustrated in Fig. 3 using the isotropic second order structure function

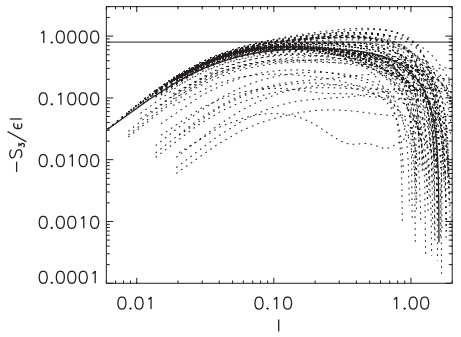

FIG. 2. Third order structure functions $-S_3(\mathbf{l})$ compensated by ϵl for the same run as in Fig. 1. The average $-S_3^{00}/\epsilon l$ is indicated by the thick solid line. The horizontal line indicates 4/5.

$G_2^{00}(l)=S_2^{00}(l)$ for runs T1, T2, and T3. The scaling in the inertial range of this function is associated with the scaling in the same range of scales of the isotropic energy spectrum. According to Kolmogorov theory (hereafter, K41) [32], the second order structure function scales as $\sim l^{\zeta_2}$ with $\zeta_2=2/3$, which implies in turn an energy spectrum $E(k)\sim k^{-(\zeta_2+1)}=k^{-5/3}$. The slope of the structure functions in Fig. 3 is slightly larger than 2/3, an effect associated to intermittency as discussed in more detail in the next section.

At this point it is worth introducing two ways to measure dispersion and errors in the determination of the exponents in the structure functions. We will use the mean square error of the exponent resulting from the least square fit, as defined, e.g., in [33]. This error we will denote as e. We will also use

$$\sigma=\left[\frac{1}{N_d}\sum_{j=1}^{N_d}(\zeta_2^{(j)}-\zeta_2)^2\right]^{1/2} \tag{10}$$

which is the standard deviation of the exponents when comparing the average value (over all directions) ζ_2 with the value obtained doing a least square fit in each direction $\zeta_2^{(j)}$. While e gives information about the quality of the fit (how much the average curve over all directions deviates from a straight line in the range of scales considered), the latter gives information about how much the exponents fluctuate

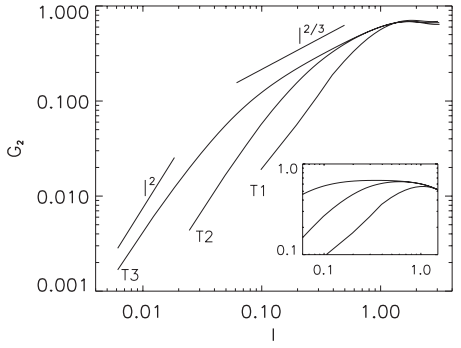

FIG. 3. Isotropic component of the second order structure function $G_2^{00}(=S_2^{00})$ for the nonhelical runs T1, T2, and T3 with increasing Reynolds number. The slopes of 2/3 and 2 are shown as references. The inset shows the three structure functions compensated by 2/3.

around their mean when considering the individual directions (as illustrated, e.g., by the dispersion in the slopes of the dotted lines in Fig. 1). From Figs. 1 and 2 it is clear that σ will be substantially larger than e.

As an example, a best fit to the power law in the second order structure function of the run T3, using the range of scales where G_3^{00} follows an approximate $\sim l$ law, gives $\zeta_2=0.702\pm0.004(0.07)$, where the notation of the error gives the mean square error e followed by the standard deviation σ between parenthesis. Remarkably, at lower resolutions we also recover deviations from the K41 prediction for ζ_2 and the energy spectrum, with run T2 giving $\zeta_2=0.69\pm0.01(0.1)$ and run T1 giving $\zeta_2=0.69\pm0.04(0.2)$. The second order isotropic structure functions for the ABC runs follow in the inertial range similar power laws, with slopes $0.67\pm0.04(0.1)$, $0.695\pm0.006(0.1)$ and $0.703\pm0.003(0.06)$, respectively, for the resolutions of 64^3, 256^3, and 1024^3 grid points. The six values are within error bars. At large Reynolds numbers, $S_2(l)^{00}$ is close to $\sim l^{-0.7}$ and the energy spectrum close to $E(k)\sim k^{-1.7}$ for both helical and nonhelical cases, which is slightly steeper than $\sim k^{-5/3}$. This result is consistent with the result obtained from the largest simulation of isotropic and homogeneous turbulence done up to the moment using 4096^3 grid points [4,34], and with other simulations at large spatial resolution and Reynolds number (see, e.g., [2]).

V. INTERMITTENCY

A. High order moments and anomalous scaling

Overall, the functions $S_p(\mathbf{l})$ and $G_p(\mathbf{l})$ for all values of p studied display, after averaging over all directions, a dissipative range that goes as $\sim l^p$, an inertial range following some power law, and a range at large scales that depends on the forcing. Each individual direction behaves as the average, although the structure functions for each direction show larger fluctuations and dispersion, specially at large scales. This can be understood in terms of anisotropies associated to the forcing which prevail at large scales. The differences between particular directions and the isotropic component decrease as the Reynolds number increases.

According to K41 theory, the longitudinal structure functions of order p should scale in the inertial range as $S_p^{00}(l)\sim l^{\xi_p}$ with $\xi_p=p/3$, where ξ_p are the scaling exponents. This scaling corresponds to a scale invariant (nonintermittent) flow. However, turbulence comes in gusts and regions with strong gradients do not fill the entire space. In practice, strong events are localized in space and time, and the probability of finding strong gradients at small scales is larger than what can be expected from a Gaussian distribution. Intermittency leads to anomalous scaling (deviations from the $\xi_p=p/3$ relation), as the higher the order the more important are the contributions from these strong events. For the energy spectrum, the scarcity of the small scales is responsible for the steeper than $k^{-5/3}$ energy spectrum discussed in the previous section.

In experiments and simulations [31] it has been observed that the generalized structure functions $G_p(l)$ scale in the same way as the $S_p(l)$ functions (with the scaling range often

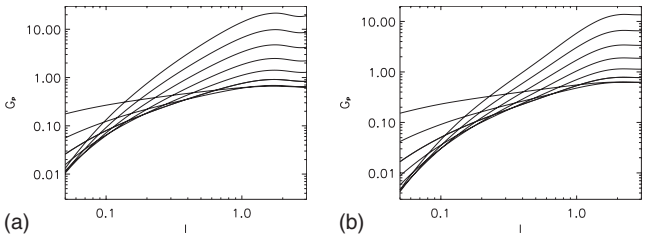

FIG. 4. Above: $G_p^{00}(l)$ structure functions as function of the increment l for p from 1 to 8 for the nonhelical T3 run. $G_3^{00}(l)$ is indicated by the thick curve. Only a range of scales near the inertial range is shown. Below: same for the isotropic generalized structure functions for the helical run A3. In both figures, the error bars correspond to the error e.

improved). Here, and following the notation of the previous section, we will denote the scaling exponents obtained for $G_p^{00}(l)$ as $G_p^{00} \sim l^{\zeta_p}$. The dependence of the $G_p^{00}(l)$ with the order is illustrated in Fig. 4. This figure shows the generalized isotropic structure functions from $p=1$ to 8 for runs T3 and A3. Only a range of scales near the inertial range is shown. In the inertial range, the longitudinal structure functions show approximate scaling laws of the form $G_p^{00}(l) \sim l^{\zeta_p}$ as expected. As p increases, the scaling exponent ζ_p increases monotonically. To check convergence of the structure functions and exponents, we computed the accumulated moments [2,3], and verified that there is convergence up to the eight order for these two runs (see, e.g., [2] for the accumulated moments in run T3 for the average in only two particular directions). For the runs with lower resolution, we computed structure functions up to the order p according to the convergence of their accumulated moments.

Let us now consider the scaling exponents ζ_p in the inertial range of all runs (where we define the inertial range as the range of scales where $G_3^{00} \sim l$ scaling holds). We start comparing the dependence of these exponents with the Reynolds number for the nonhelical runs. Figure 5 shows ζ_p from the isotropic generalized structure functions for the three runs with TG forcing. The $\zeta_p = p/3$ linear relation is indicated by the straight line. As previously mentioned, deviations of the ζ_p exponents from the straight line are an indication of intermittency. Remarkably, the scaling exponents for the runs at lower Reynolds number are closer to the straight line than the exponents of the run at the largest Reynolds number, indicating intermittency still increases with the scale separation in the range of Reynolds numbers studied, and that more spatial resolution is required to reach convergence with Reynolds number for high order moments. Figure 5 also shows the same results for the ABC runs. For this flow, a similar dependence of the exponents with the Reynolds number can be identified.

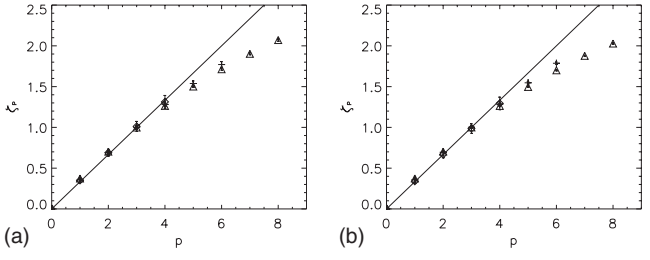

FIG. 5. Above: scaling exponents ζ_p in the nonhelical runs with increasing Reynolds number T1 (diamonds), T2 (crosses), and T3 (triangles). The K41 prediction is given as reference. Below: same exponents for the helical runs A1 (diamonds), A2 (crosses), and A3 (triangles).

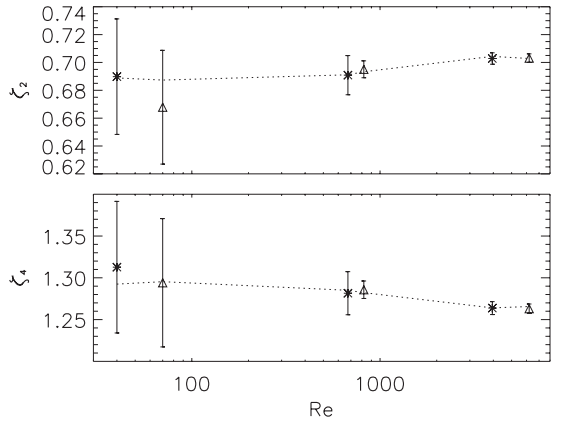

FIG. 6. Second order (above) and fourth order (below) scaling exponents as a function of the Reynolds number for all runs (triangles are for helical forcing and crosses for nonhelical forcing). Error bars correspond to the error e. The dotted line shows the same exponents using ESS.

Figure 6 shows the dependence of the second and fourth order scaling exponents for all runs as a function of the Reynolds number. Because of the different forcing functions used, even when comparing runs at the same resolutions the Reynolds numbers are slightly different. The second order exponent ζ_2 slowly grows with Re, and seems to saturate for the largest Reynolds numbers reached. Note however that all values are within error bars (based on the error e). For ζ_4 a decrease with the Reynolds number is observed, and in this case not all values are within error bars. The increase of the intermittency with Reynolds number is more pronounced when the intermittency exponent $\mu = 2\zeta_3 - \zeta_6$ is studied as a function of Re (see Fig. 7; only the runs at larger Reynolds numbers are shown, as determination of μ requires the sixth order exponent). For the runs at the larger spatial resolution

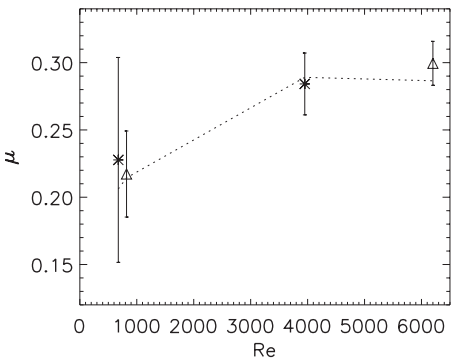

FIG. 7. Intermittency exponent as a function of the Reynolds number for the four runs at larger Reynolds number (labels as in Fig. 6). As in Fig. 6, the dotted line show the intermittency exponent when ESS is used.

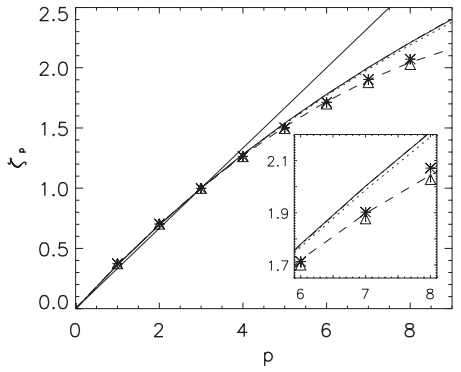

FIG. 8. Comparison between the ζ_p exponents from the nonhelical T3 (crosses) and helical A3 runs (triangles). Shown as a reference are the K41 (solid straight line), log-normal (dash), mean field (dotted), She-Leveque (dash-dotted), and Arimitsu and Arimitsu (solid) predictions. The mean-field model and Arimitsu and Arimitsu model are indistinguishable. The inset shows a zoom for the highest order moments, with error bars based on the error e.

we obtain $\mu=0.28\pm0.02$ and $\mu=0.30\pm0.01$, respectively, for T3 and A3, while for runs T2 and A2 we find $\mu=0.23\pm0.07$ and $\mu=0.22\pm0.03$, respectively. Our values for the highest Reynolds numbers agree with measurements made by Meneveau and Sreenivasan [35] where they obtained $\mu=0.26\pm0.03$ (see also [36]).

B. Role of helicity

To study whether previously reported differences between helical and nonhelical isotropic and homogeneous turbulence are associated to the presence of helicity or to anisotropies related to the forcing functions, we now focus on the data sets with the largest spatial resolution. Figure 8 shows the scaling exponents ζ_p as a function of p up to the eight order for runs T3 and A3. The K41 prediction is shown as a reference, together with different models of intermittency: the log-normal model [37],

$$\zeta_p = \frac{p}{3} + \frac{\mu}{18}(3p - p^2); \tag{11}$$

where μ is the intermittency exponent previously defined, the She-Leveque model [38],

$$\zeta_p = \frac{p}{9} + 2\left[1 - \left(\frac{2}{3}\right)^{p/3}\right]; \tag{12}$$

the mean-field approximation [39]

$$\zeta_p = \frac{1.15}{3(1+0.05p)}p; \tag{13}$$

and the model of Arimitsu and Arimitsu [40,41],

$$\zeta_p = \frac{\alpha_0 p}{3} - \frac{2Xp^2}{9(1+C_{p/3}^{1/2})} - \frac{1}{1-q}[1-\log_2(1+C_{p/3}^{1/2})], \tag{14}$$

where

TABLE II. Comparison of scaling exponents in helical and nonhelical flows at the largest Reynolds number studied; p is the order, ζ_{A3} are the isotropic scaling exponents of the helical run, ζ_{T3} are the exponents of the nonhelical run, and $\zeta_{A3}-\zeta_{T3}$ is their difference.

p	ζ_{T3}	ζ_{A3}	$\zeta_{A3}-\zeta_{T3}$
1	0.372 ± 0.002	0.373 ± 0.001	0.001 ± 0.003
2	0.702 ± 0.004	0.703 ± 0.003	0.000 ± 0.007
3	0.998 ± 0.005	0.999 ± 0.004	0.00 ± 0.01
4	1.263 ± 0.007	1.263 ± 0.005	-0.00 ± 0.01
5	1.500 ± 0.009	1.495 ± 0.006	-0.00 ± 0.01
6	1.71 ± 0.01	1.700 ± 0.007	-0.01 ± 0.01
7	1.90 ± 0.01	1.877 ± 0.008	-0.02 ± 0.02
8	2.07 ± 0.01	2.028 ± 0.009	-0.04 ± 0.02

$$C_{p/3} = 1 + 2\left(\frac{p}{3}\right)^2(1-q)X\ln(2), \tag{15}$$

and the quantities α_0, X, and q are determined from the intermittency exponent μ following the expressions in Refs. [40,41].

The She-Leveque model and the mean-field approximation have no free parameters, while the log-normal model and the model of Arimitsu and Arimitsu depend solely on the intermittency exponent. For the log-normal model, we use $\mu=0.28$ which is compatible with the value found in the A3 and T3 runs and also consistent with experimental results [35]. Arimitsu and Arimitsu state that for infinite Reynolds number $\mu=0.22$ should be used in their model, and in [41] give explicit values for α_0, X, and q for this case. These are the values we use in Fig. 8, and when plotting the model with values corresponding to larger values of μ we observed an improvement in the model although measurable differences for the highest orders persist. The best fit to the data is given by the log-normal model, although it is well known that for higher order moments the model will fail as its exponents do not increase monotonically with p. The data deviates from all the models.

Table II shows a comparison of the ζ_p exponents of the isotropic sector for the helical and nonhelical runs at the largest spatial resolution. Except for the highest order computed, differences are within error bars, indicating that previously reported differences measured without the SO(3) decomposition were associated to contributions from the anisotropic sector. The small discrepancy observed for $p=8$ may be related to Reynolds number dependence, as runs A3 has a slightly larger Reynolds number than run T3, and as it was noted before, the higher order exponents slowly decrease as the Reynolds number is increased. Other possible causes for this dependence are considered in the next section.

VI. EXTENDED SELF-SIMILARITY AND COMPARISON OF SCALING EXPONENTS

So far we have studied the scaling laws corresponding mostly to the generalized structure functions $G_p(l)=A_p l^{\zeta_p}$. As mentioned before, it was observed [31] that these functions

TABLE III. Scaling exponents ξ (without absolute values), ζ (with absolute values), ξ^{ESS}, and ζ^{ESS} (same as ξ and ζ but also using ESS) for the nonhelical run at the larger resolution T3, as a function of the order p. The exponents from the She-Leveque model are given as a reference.

p	ξ_{T3}	ζ_{T3}	ξ^{ESS}_{T3}	ζ^{ESS}_{T3}	She-Leveque model
1		$0.372 \pm 0.002(0.04)$		$0.3721 \pm 0.0001(0.008)$	0.364
2	$0.749 \pm 0.003(0.07)$	$0.702 \pm 0.004(0.07)$	$0.7027 \pm 0.0001(0.008)$	$0.7043 \pm 0.0001(0.007)$	0.696
3	$0.999 \pm 0.004(0.2)$	$0.998 \pm 0.005(0.1)$	1	1	1
4	$1.356 \pm 0.006(0.1)$	$1.263 \pm 0.007(0.1)$	$1.2664 \pm 0.0001(0.01)$	$1.2640 \pm 0.0001(0.01)$	1.280
5	$1.570 \pm 0.007(0.4)$	$1.500 \pm 0.009(0.1)$	$1.419 \pm 0.003(0.1)$	$1.5000 \pm 0.0002(0.03)$	1.538
6	$1.851 \pm 0.007(0.1)$	$1.71 \pm 0.01(0.1)$	$1.7190 \pm 0.0004(0.06)$	$1.7109 \pm 0.0004(0.05)$	1.778
7	$2.039 \pm 0.008(0.6)$	$1.90 \pm 0.01(0.2)$	$1.846 \pm 0.003(0.2)$	$1.8992 \pm 0.0006(0.07)$	2.001
8	$2.251 \pm 0.009(0.1)$	$2.07 \pm 0.01(0.2)$	$2.0797 \pm 0.0008(0.1)$	$2.0667 \pm 0.0008(0.09)$	2.210

follow scaling laws similar to the ones followed by the structure functions $S_p(l) = B_p l^{\xi_p}$. Moreover, there is an alternative way to express these scaling laws using the Kolmogorov 4/5 law

$$G_p(l) = A'_p [G_3(l)]^{\xi^{ESS}_p}, \tag{16}$$

or

$$S_p(l) = B'_p [G_3(l)]^{\xi^{ESS}_p}; \tag{17}$$

experiments and numerical data show that when these expressions are used the range of scales where power laws are observed grows significantly (see, e.g., [31]). This is often referred to as extended self-similarity (ESS) [24,25]. In this section, we compare in more detail the scaling exponents ζ_p and ξ_p (with and without absolute values; i.e., corresponding, respectively, to the functions G_p and S_p), and the exponents resulting from the ESS analysis ζ^{ESS}_p and ξ^{ESS}_p, for the runs at the larger resolution (T3 and A3). Note that G_3 is often used in ESS [see Eqs. (16) and (17)] instead of S_3 as the reference function that scales linearly with l.

Table III shows ζ, ξ, ζ^{ESS}, and ξ^{ESS} for run T3, while Table IV shows the same exponents for run A3. Note that ξ_p and ζ_p differ for even values of p as different ranges of scales are used depending, respectively, on the range for which $S^{00}_p \sim l$ or $G^{00}_p \sim l$ holds. We explicitly give the ranges of scales used for the fit in each simulation in Table V. The ranges substantially increase as ξ_p, ζ_p, ξ^{ESS}_p, and ζ^{ESS}_p are computed (as a reference, the forcing acts at $L_f \approx 2$, and the smallest resolved scale is ≈ 0.006 in both runs).

Two comments are in order. First, when the exponents are computed without absolute values and without ESS (ξ_p), large fluctuations are observed in each direction for odd values of p, which results in a large dispersion σ. However, the ξ_p exponents are in some cases closer to the values from the She-Leveque model. Second, in the other cases and even after using ESS, the exponents are more intermittent than what is predicted by the She-Leveque model (see [3] for similar results using isotropic random forcing). However, the use of ESS makes the dependence of the exponents with the Reynolds number decrease (specially for small Reynolds numbers) as has been reported before [24,25,31]. This is illustrated by the dotted line in Figs. 6 and 7.

VII. CONCLUSIONS

In this work we studied scaling exponents and intermittency in the isotropic sector of turbulent flows at different Reynolds numbers, generated by Taylor-Green forcing and by Arn'old-Beltrami-Childress forcing. The first is nonhelical while the latter is maximally helical. The spatial resolutions were 64^3, 256^3, and 1024^3 grid points, with the Reynolds number (based on the integral scale) ranging from 40 to 6200.

A dependence of the intermittency corrections with the Reynolds number was found, with a larger intermittency ex-

TABLE IV. Scaling exponents ξ, ζ, ξ^{ESS}, and ζ^{ESS} as in Table III but for the helical run at the larger resolution A3.

p	ξ_{A3}	ζ_{A3}	ξ^{ESS}_{A3}	ζ^{ESS}_{A3}	She-Leveque model
1		$0.373 \pm 0.001(0.03)$		$0.3706 \pm 0.0002(0.007)$	0.364
2	$0.703 \pm 0.003(0.07)$	$0.703 \pm 0.003(0.06)$	$0.7027 \pm 0.0004(0.008)$	$0.7028 \pm 0.0001(0.007)$	0.696
3	$0.999 \pm 0.004(0.2)$	$0.999 \pm 0.004(0.08)$	1	1	1
4	$1.311 \pm 0.006(0.09)$	$1.263 \pm 0.005(0.1)$	$1.264 \pm 0.001(0.01)$	$1.2656 \pm 0.0001(0.01)$	1.280
5	$1.545 \pm 0.006(0.2)$	$1.495 \pm 0.006(0.1)$	$1.430 \pm 0.003(0.1)$	$1.5027 \pm 0.0003(0.03)$	1.538
6	$1.764 \pm 0.008(0.1)$	$1.700 \pm 0.007(0.1)$	$1.7072 \pm 0.0004(0.06)$	$1.7135 \pm 0.0006(0.05)$	1.778
7	$1.978 \pm 0.008(0.8)$	$1.877 \pm 0.008(0.1)$	$1.854 \pm 0.002(0.1)$	$1.900 \pm 0.001(0.08)$	2.001
8	$2.09 \pm 0.01(0.1)$	$2.028 \pm 0.009(0.2)$	$2.046 \pm 0.001(0.1)$	$2.064 \pm 0.001(0.1)$	2.210

TABLE V. Ranges of scales used to compute the scaling exponents in Tables III and IV, in units of the box size (2π) for runs T3 (nonhelical) and A3 (helical). As a reference, the forcing acts at $L_f \approx 2$ and the smallest resolved scale is ≈ 0.006 in both runs.

Run	ξ	ζ	ξ^{ESS}	ζ^{ESS}
T3	0.15–0.26	0.11–0.59	0.04–0.56	0.03–1.50
A3	0.16–0.24	0.11–0.65	0.04–0.68	0.03–1.42

ponent as the Reynolds number was increased. When the SO(3) decomposition was used, no dependence of the level of intermittency with the helicity content in the flow was observed, and small differences at the highest order studied may be due to Reynolds number dependence of the exponents or to sensitivity of the fitting.

When comparing with models of intermittency in the literature, it was found that the data are more intermittent than predictions from the She-Leveque model, the mean-field approximation, and the model of Arimitsu and Arimitsu. In spite of the well known problems with the log-normal model, this model gives the best fit to our data (however, it should be remarked that the log-normal model will fail to fit higher order moments than the ones computed here). It is unclear to us what is the origin of the strong intermittency observed, but we note that similar results were also reported in numerical simulations using isotropic random forcing [3]. In this context, it is interesting to question the need to develop new models of intermittency without better data or a deeper understanding of the origin of intermittency in homogeneous and isotropic turbulent flows.

Using absolute values in the definition of the structure functions or using ESS substantially decreases errors in the determination of the exponents. Overall, the combination of SO(3), ESS, and the high spatial resolution of the simulations makes the errors e of the least square fit too small to extract from them information beyond the goodness of the fit for a particular snapshot of the velocity field. Fluctuations of the exponents for the increments in different spatial directions, quantified by the dispersion σ, are substantially larger and the errors of the exponents are in practice bounded between e and σ. The comparison between the exponents and errors thus obtained gives some information on the sensitivity of the exponents with the fitting range. Finally, when ESS is used the dependence of the exponents with the Reynolds number is decreased, specially for the runs at lower Reynolds number.

ACKNOWLEDGMENTS

The authors would like to acknowledge comments by anonymous referees that helped them substantially improve the presentation. The authors also acknowledge support from Secretaria de Ciencia y Tecnica, UBA, Grant No. UBACYT X468/08 and Agencia Nacional de Promocion Cientifica y Tecnologica, Grant No. PICT-2007-02211. P.D.M. acknowledges support from the Carrera del Investigador Científico of CONICET.

[1] U. Frisch, *Turbulence: The Legacy of A.N. Kolmogorov* (Cambridge University Press, Cambridge, England, 1995).
[2] P. D. Mininni, A. Alexakis, and A. Pouquet, Phys. Rev. E **77**, 036306 (2008).
[3] T. Gotoh, D. Fukayama, and T. Nakano, Phys. Fluids **14**, 1065 (2002).
[4] Y. Kaneda, T. Ishihara, M. Yokokawa, K. Itakura, and A. Uno, Phys. Fluids **15**, L21 (2003).
[5] P. D. Mininni, A. Alexakis, and A. Pouquet, Phys. Rev. E **74**, 016303 (2006).
[6] V. Borue and S. A. Orszag, Phys. Rev. E **55**, 7005 (1997).
[7] Q. Chen, S. Chen, G. L. Eyink, and D. D. Holm, Phys. Rev. Lett. **90**, 214503 (2003).
[8] Q. Chen, S. Chen, and G. L. Eyink, Phys. Fluids **15**, 361 (2003).
[9] D. O. Gómez and P. D. Mininni, Physica A **342**, 69 (2004).
[10] S. Kurien, M. A. Taylor, and T. Matsumoto, J. Fluid Mech. **515**, 87 (2004).
[11] L. Biferale, D. Pierotti, and F. Toschi, Phys. Rev. E **57**, R2515 (1998).
[12] I. Arad, V. S. Lvov, and I. Procaccia, Phys. Rev. E **59**, 6753 (1999).
[13] I. Arad, B. Dhruva, S. Kurien, V. S. Lvov, I. Procaccia, and K. R. Sreenivasan, Phys. Rev. Lett. **81**, 5330 (1998).
[14] L. Biferale and I. Procaccia, Phys. Rep. **414**, 43 (2005).
[15] M. A. Taylor, S. Kurien, and G. L. Eyink, Phys. Rev. E **68**, 026310 (2003).
[16] S. Kurien and K. R. Sreenivasan, Phys. Rev. E **62**, 2206 (2000).
[17] L. Biferale and M. Vergassola, Phys. Fluids **13**, 2139 (2001).
[18] L. Biferale and F. Toschi, Phys. Rev. Lett. **86**, 4831 (2001).
[19] L. Biferale, I. Daumont, A. Lanotte, and F. Toschi, Phys. Rev. E **66**, 056306 (2002).
[20] G. Eyink, Nonlinearity **16**, 137 (2003).
[21] L. Biferale, E. Calzaverini, F. Toschi, and R. Tripiccione, Europhys. Lett. **64**, 461 (2003).
[22] L. Biferale, E. Calzaverini, A. S. Lanotte, F. Toschi, and R. Tripiccione, Physica A **338**, 194 (2004).
[23] L. Biferale, I. Daumont, A. Lanotte, and F. Toschi, Eur. J. Mech. B/Fluids **23**, 401 (2004).
[24] R. Benzi, S. Ciliberto, R. Tripiccione, C. Baudet, F. Massaioli, and S. Succi, Phys. Rev. E **48**, R29 (1993).
[25] R. Benzi, S. Ciliberto, C. Baudet, G. Ruiz Chavarria, and R. Tripiccione, Europhys. Lett. **24**, 275 (1993).
[26] D. O. Gómez, P. D. Mininni, and P. Dmitruk, Adv. Space Res. **35**, 899 (2005).
[27] D. O. Gómez, P. D. Mininni, and P. Dmitruk, Phys. Scr. T **116**, 123 (2005).
[28] G. I. Taylor and A. E. Green, Proc. R. Soc. London, Ser. A **158**, 499 (1937).
[29] S. Childress and A. D. Gilbert, *Stretch, Twist, Fold: The Fast Dynamo* (Springer-Verlag, Berlin, 1999).

[30] A. Alexakis, P. D. Mininni, and A. Pouquet, Phys. Rev. Lett. **95**, 264503 (2005).
[31] A. Arneodo, C. Baudet, F. Belin, R. Benzi, B. Castaing, B. Chabaud, R. Chavarria, S. Ciliberto, R. Camussi, F. Chilla, B. Dubrulle, Y. Gagne, B. Hebral, J. Herweijer, M. Marchand, J. Maurer, J. F. Muzy, A. Naert, A. Noullez, J. Peinke, F. Roux, P. Tabeling, W. van de Water, and H. Willaime, Europhys. Lett. **34**, 411 (1996).
[32] A. N. Kolmogorov, Dokl. Akad. Nauk SSSR **30**, 299 (1941).
[33] W. H. Press, B. P. Flannery, S. A. Teukolsky, and W. T. Vetterling *Numerical Recipes in FORTRAN 77* (Cambridge University Press, Cambridge, England, 1992).
[34] T. Ishihara, T. Gotoh, and Y. Kaneda, Annu. Rev. Fluid Mech. **41**, 165 (2009).
[35] C. Meneveau and K. R. Sreenivasan, J. Fluid Mech. **224**, 429 (1991).
[36] K. R. Sreenivasan and P. Kailasnath, Phys. Fluids A **5**, 512 (1993).
[37] A. N. Kolmogorov, J. Fluid Mech. **13**, 82 (1962).
[38] Z. S. She and E. Leveque, Phys. Rev. Lett. **72**, 336 (1994).
[39] V. Yakhot, Phys. Rev. E **63**, 026307 (2001).
[40] T. Arimitsu and N. Arimitsu, Phys. Rev. E **61**, 3237 (2000).
[41] T. Arimitsu and N. Arimitsu, Physica A **295**, 177 (2001).